Acoustic radiation of MEMS and NEMS resonators in fluids

Cite as: J. Appl. Phys. **129**, 064304 (2021); https://doi.org/10.1063/5.0037959 Submitted: 17 November 2020 . Accepted: 28 January 2021 . Published Online: 11 February 2021

🗓 Alyssa T. Liem, Chaoyang Ti, Vural Kara, Atakan B. Ari, J. Gregory McDaniel, and 🗓 Kamil L. Ekinci







ARTICLES YOU MAY BE INTERESTED IN

Profilometry and stress analysis of suspended nanostructured thin films

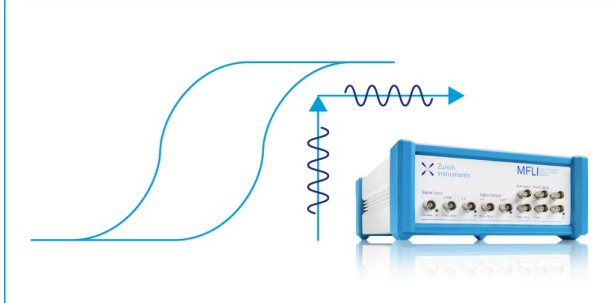
Journal of Applied Physics 129, 065302 (2021); https://doi.org/10.1063/5.0037406

A comprehensive model and numerical analysis of electron mobility in GaN-based high electron mobility transistors

Journal of Applied Physics 129, 064303 (2021); https://doi.org/10.1063/5.0037228

Flexoelectric barium strontium titanate (BST) hydrophones

Journal of Applied Physics 129, 064504 (2021); https://doi.org/10.1063/5.0038756



Webinar How to Characterize Magnetic Materials Using Lock-in Amplifiers





Register now



Acoustic radiation of MEMS and NEMS resonators in fluids

Cite as: J. Appl. Phys. **129**, 064304 (2021); doi: 10.1063/5.0037959 Submitted: 17 November 2020 · Accepted: 28 January 2021 · Published Online: 11 February 2021







Alyssa T. Liem,^{1,a)} Chaoyang Ti,^{1,2,b)} Vural Kara,^{1,2,c)} Atakan B. Ari,^{1,2,d)} J. Gregory McDaniel,^{1,e)} and Kamil L. Ekinci^{1,2,f)}

AFFILIATIONS

- Department of Mechanical Engineering, Boston University, Boston, Massachusetts 02215, USA
- ²Divisions of Materials Science and Engineering and the Photonics Center, Boston University, Boston, Massachusetts 02215, USA
- a)Author to whom correspondence should be addressed: atliem@bu.edu
- b)Electronic mail: chaoyang@bu.edu
- c) Present address: Saint-Gobain Research North America, Northborough, Massachusetts 01532, USA
- d)Electronic mail: atakaba@bu.edu
- e)Electronic mail: jgm@bu.edu
- f)Electronic mail: ekinci@bu.edu

ABSTRACT

Here, we study the acoustic radiation generated by the vibration of miniaturized doubly clamped and cantilever beam resonators in viscous fluids. Acoustic radiation results in an increase in dissipation and consequently a decrease in the resonator's quality factor. We find that dissipation due to acoustic radiation is negligible when the acoustic wavelength in the fluid is much larger than the bending wavelength. In this regime, dissipation is primarily due to the viscous losses in the fluid and may be predicted with the two-dimensional cylinder approximation in the absence of axial flow and substrate effects. In contrast, when the bending wavelength approaches the length of the acoustic wavelength, acoustic radiation becomes prominent. In this regime, dissipation due to acoustic radiation can no longer be neglected, and the cylinder approximation inaccurately characterizes the total energy loss in the system. Experiments are performed with microcantilevers of varying lengths in Ar and N_2 to observe trends in the acoustic wavelength of the fluid and bending wavelength. Additional experimental results from doubly clamped nanoelectromechanical system beams are also presented. Experimental results illustrate an increase in dissipation, which is further analyzed with the use of three-dimensional finite element models. With the numerical simulations, we calculate the radiation efficiency of the measured devices and analyze the pressure fields generated by the vibrating resonators. This analysis allows one to estimate the effects of acoustic radiation for any resonator.

Published under license by AIP Publishing. https://doi.org/10.1063/5.0037959

I. INTRODUCTION

In the last few decades, miniaturized mechanical resonators have gained significant attention due to their unprecedented sensing abilities. Microelectromechanical system (MEMS) resonators, and the even smaller nanoelectromechanical system (NEMS) resonators, with sub-micrometer linear dimensions, have found numerous applications in sensing biological and physical quantities inside fluids, commonly air and water, including the mass of adsorbed molecules, ^{1,2} the random motion of adsorbed bacteria, ³ the added dissipation from a fluid, ⁴ and turbulent pressure fluctuations. ⁵ Hence, much attention has been placed on understanding the dissipation

due to the fluid-structure coupling. Specifically, many have studied the dissipation due to viscous losses in the fluid, which can be predicted by solving the linearized incompressible Navier-Stokes (NS) equations. Most notable is the two-dimensional (2D) cylinder approximation, which approximates a slender vibrating structure, such as a doubly clamped beam or cantilever, as an oscillating cylinder in an infinite viscous fluid. An expression for the fluid force applied to the structure is found in terms of the hydrodynamic function derived by Stokes in 1851. An extension to the 2D cylinder approximation is the 2D blade approximation, which accounts for the rectangular cross section of a beam.

Experimental work presented by Chon *et al.*⁸ and Yu-Hang and Wen-Hao⁹ validated the 2D approximation's accuracy in predicting the resonant frequency and quality factor (*Q*) of resonators vibrating in low bending modes. Limitations in the approximation were also found with experimental work and numerical studies, where inaccuracies due to the presence of either axial flow or squeeze film effects were found. ^{10–13} In summary, the previous work found that the 2D cylinder approximation, derived for an incompressible viscous fluid, accurately predicts dissipation of a miniaturized resonator vibrating in a viscous fluid when axial flow and squeeze film effects are negligible.

Due to the small linear dimensions of MEMS and NEMS devices, previous work often assumed that acoustic radiation was negligible^{6,14} and only considered viscous losses when predicting dissipation. Recently, acoustic losses of circular plate resonators have been studied. Vishwakarma et al. 15 studied dissipation due to squeeze film damping and acoustic radiation in a prestressed drumhead resonator operating in air. Their work predicted the total dissipation for the first 15 transverse vibration modes by summing the dissipation due to squeeze film damping and acoustic losses. Their work concluded that squeeze film damping dominated at low frequencies, while acoustic losses dominated at high frequencies. Similarly, Gil-Santos et al. 16 analyzed nanooptomechanical disks vibrating in their mechanical radial breathing modes. Their work analyzed dissipation due to viscous losses and acoustic radiation for disks with varying radii operating in different liquids. Their work also looked at the net dissipation when comparing predictions to experimental measurements. Although both works presented methods for predicting dissipation due to acoustic radiation, it remains unclear when such losses become prominent and when they may be neglected.

In this paper, a dimensionless parameter that may be computed for any resonator, the wavenumber ratio, is introduced and used to analyze trends in dissipation for MEMS and NEMS resonators. Experimental results showing dissipation due to acoustic radiation from vibrating microcantilevers and doubly clamped NEMS beams are presented. With supporting numerical simulations of three-dimensional (3D) finite element models (FEMs), measurements show that resonators radiate sound when the bending wavelength approaches the acoustic wavelength. It is found that this often occurs at higher bending modes and, therefore, higher frequencies due to the bending and acoustic wavelengths' dependencies on frequency. The acoustic wavelength is proportional to the inverse of frequency, whereas the bending wavelength is proportional to the inverse of the square root of frequency. As a result, in the measurements presented, acoustic radiation becomes prominent at higher bending modes where the bending wavelength is of comparable magnitude to the acoustic wavelength. Here, the acoustic and bending wavelength are compared via the wavenumber ratio.

In the present work, acoustic radiation is identified by comparing the measured dissipation to the dissipation predicted by the 2D viscous approximation. When acoustic radiation is negligible as well as axial flow and substrate effects, it is found that the measured dissipation agrees well with that predicted by the viscous approximation. However, when acoustic radiation becomes prominent, a departure from the viscous approximation is observed. Numerical FEM simulations are also analyzed to predict the resonators' radiation

efficiency and the resulting pressure fields. Results show that an increase in dissipation corresponds to an increase in radiation efficiency. When radiation efficiency is relatively large, the vibrating resonator is able to radiate sound and generate pressure waves in the fluid, resulting in energy being transferred from the structure to the compressible fluid. Analysis of the measured dissipation's dependence on pressure is presented to distinguish between dissipation due to viscous losses and dissipation due to acoustic radiation. Furthermore, various resonators with different lengths and mechanical properties are measured and analyzed in different fluids to observe trends in the wavenumber ratio.

The results presented in this paper show that miniaturized resonators with small linear dimensions may radiate sound if the bending wavelength approaches the acoustic wavelength. Measurements from microcantilevers and doubly clamped NEMS beams that radiate sounds are presented. The presence of acoustic radiation results in an increase in dissipation that may not be predicted by approximations that consider the fluid to be incompressible.

II. TWO-DIMENSIONAL VISCOUS DISSIPATION APPROXIMATION

In this section, the 2D cylinder approximation is briefly reviewed. The 2D approximation will be later used to predict the dissipation of MEMS and NEMS beams vibrating in viscous fluids. The approximation is derived from the incompressible linearized NS equations and assumes the fluid is of infinite extent. For slender bodies whose length L is much greater than its width b and thickness h, such as microcantilevers and NEMS beams, the structure is approximated as a long cylinder with diameter b oscillating perpendicular to its axis but in the mode shape of the structure. The approximation predicts the force applied by the fluid to the beam in terms of the hydrodynamic function $\Gamma_{\rm circ}$. The resulting dissipation is approximated as 6,17

$$\frac{1}{Q} \approx \frac{\Gamma''_{\text{circ}}(\alpha)}{\frac{1}{T_0} + \Gamma'_{\text{circ}}(\alpha)},\tag{1}$$

where Q is the quality factor, and $\Gamma'_{\rm circ}$ and $\Gamma''_{\rm circ}$ are the real and imaginary part, respectively, of the hydrodynamic function, $\Gamma_{\rm circ}$. The analytical expression for the hydrodynamic function is ^{7,18,19}

$$\Gamma_{\rm circ}(\alpha) = 1 + \frac{4iK_1(-i\sqrt{i\alpha})}{\sqrt{i\alpha}K_0(-i\sqrt{i\alpha})},\tag{2}$$

where K_0 and K_1 are the zeroth and first order modified Bessel functions of the second kind. The argument of $\Gamma_{\rm circ}$ is in terms of the Reynolds number

$$\alpha = \frac{\rho_0 \omega b^2}{4\mu},\tag{3}$$

where ρ_0 and μ are the density and dynamic viscosity of the fluid, respectively, and ω is the angular frequency of oscillation. In Eq. (1), T_0 is a mass loading parameter equal to the ratio of the mass of cylinder of fluid to the mass of the beam, ²⁰ such that

$$T_0 = \frac{\pi \rho_0 \ b}{4 \ \rho_s h},\tag{4}$$

where ρ_s is the density of the solid beam. For gas experiments, T_0 is very small, 21 such that $1/T_0 \gtrsim 1000 \gg \Gamma_{\rm circ}'$, and the dissipation may be further approximated as

$$\frac{1}{O} \approx T_0 \Gamma_{\rm circ}''(\alpha). \tag{5}$$

To account for the rectangular cross section of a beam, one can apply a small Reynolds number-dependent correction factor, $\Omega(\alpha)$, of order one to Γ_{circ} and find the hydrodynamic function of the so-called oscillating blade⁶

$$\Gamma_{\text{rect}}(\alpha) = \Omega(\alpha)\Gamma_{\text{circ}}(\alpha).$$
 (6)

The hydrodynamic function in Eq. (6) may then be used to predict the dissipation in Eq. (1) by simply replacing Γ'_{circ} and Γ''_{circ} with Γ'_{rect} and Γ''_{rect} .

III. EXPERIMENTAL MEASUREMENTS

A. Microcantilevers

Experiments with microcantilevers were carried out with commercially available tipless silicon microcantilevers from MikroMasch (NSC36). Three microcantilevers of varying length were used in the experiments, resulting in varying bending wavelengths. The dimensions of the three microcantilevers used in the experiments are listed in Table I and a schematic of the microcantilever is depicted in Fig. 1(a). There were no close-by walls or substrates in the vicinity of the microcantilever to affect the flow. The cantilevers were measured in high-purity Ar and N_2 . The properties of these gases at Standard Temperature and Pressure (STP) are listed in Table II. In the experiments, the cantilevers were excited with a sinusoidal force, such that the cantilever would oscillate at angular frequency ω . The driving frequencies were chosen near resonances of the cantilever to excite different bending modes. Table III summarizes the parameters of the conducted experiments.

For each experiment, the mean background pressure p_0 of the gas was changed, and the total dissipation $1/Q_t$ was measured. To obtain the gas dissipation, $1/Q_g$, we calculate $1/Q_g = (1/Q_t) - (1/Q_0)$, where $1/Q_0$ is the intrinsic dissipation (obtained at the lowest p_0). By changing the pressure p_0 , the density of the gas is changed by

$$\rho_0 = \frac{p_0 M}{RT},\tag{7}$$

where $R=8.3145\,\mathrm{J/mol}\,K$ is the universal gas constant, T is the temperature, and M is the molar mass of the gas. As a result, the Reynold number α varies with pressure by virtue of Eqs. (3) and (7). By measuring the dissipation at different pressures and thus different densities and Reynolds numbers, the dominant physical dissipation mechanism may be observed. When viscous losses of the gas dominate, the dissipation will vary with Reynolds number as predicted by Eq. (5). However, when acoustic radiation is present, a different trend in Reynolds number will be observed.

TABLE I. Dimensions of microcantilevers used in experiment.

	Length (µm)	Width (µm)	Thickness (µm)
Cantilever A Cantilever B	130 90	32.5 32.5	1.2 1.2
Cantilever C	110	32.5	1.2

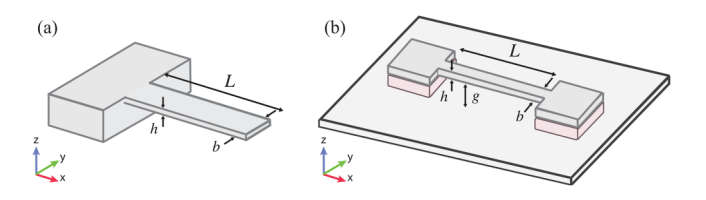


FIG. 1. Schematic of (a) a microcantilever and (b) a doubly clamped NEMS beam with a substrate.

TABLE II. Properties of gas used in experiment.

Gas	Speed of sound (m/s)	Molar mass (g/mol)	Density at STP (kg/m³)	Dynamic viscosity at STP (Pas)
Ar N ₂	319 349	39.948 28.014	1.6607 1.1644	2.23×10^{-5} 1.7436×10^{-5}
N ₂ Air	349	28.014	1.1644	1.7436 × 1.8140 ×

TABLE III. Description of conducted experiments with microcantilevers.

Cantilever	Mode number	Gas	Frequency (kHz)
A	3	Ar	2439.15
A	4	Ar	4673.20
A	5	Ar	7520.00
A	1	N_2	143.00
A	3	N_2	2438.00
A	4	N_2	4670.00
A	5	N_2	7520.00
В	2	Ar	1311.41
В	3	Ar	3564.26
В	4	Ar	6737.80
C	3	Ar	1762.39
C	4	Ar	3397.05
C	5	Ar	5516.00
C	1	N_2	103.00
C	2	N_2	638.00
C	3	N_2	1762.00
C	4	N_2	3396.00
С	5	N_2	5512.00

B. Nanomechanical beams

Experiments were also performed on nanomechanical silicon nitride Doubly clamped beam resonators with tension in air at atmospheric pressure. Figure 1(b) shows a schematic of the beam with length L, width b, thickness h, and a gap distance g between the beam and substrate. In the experiment, measurements were taken at discrete frequencies near resonance, and a modal fit was performed to find the natural frequencies and dissipation of the beam. When the details on the device and measurement process may be found in work published by Ari et al. 23

Two NEMS beam resonators were measured. The two beams mainly differed by the magnitude of tension. The first beam, which will be referred to as the low tension beam, has a tension force of $P=8.7\,\mu\text{N}$, and linear dimensions $L\times b\times h\approx 50\,\mu\text{m}\times 950\,\text{nm}\times 93\,\text{nm}$. The second beam, which will be referred to as the high tension beam, has a tension force of $P=71.3\,\mu\text{N}$ and linear dimensions $L\times b\times h\approx 50\,\mu\text{m}\times 900\,\text{nm}\times 100\,\text{nm}$. Both beams have a $g\approx 2\,\mu\text{m}$ gap between the beam and the substrate. The first ten modes of the low tension beam were measured, and the first five modes of the high tension beam were measured. Table IV lists the natural frequencies of the low tension and high tension beams.

IV. NUMERICAL METHODS

A. Three-dimensional finite element model

In the present work, the response and dissipation of the microcantilevers will also be predicted with 3D FEMs. All FEMs are constructed and analyzed using commercial software COMSOL Multiphysics*. ²⁴ In order to separate dissipation mechanisms, two FEMs, FEM1 and FEM2, are analyzed in the present work and are depicted in Fig. 2. FEM1 will include and model all linear dissipation mechanisms, whereas FEM2 models the fluid as lossless

TABLE IV. Measured natural frequencies of doubly clamped NEMS beams. The low tension beam data were taken from experimental results published by Liem *et al.*¹³

NEMS beam	Mode number	Frequency (MHz)	Wave number ratio
Low tension	1	1.8710	0.5024
Low tension	2	3.7825	0.5099
Low tension	3	5.7848	0.5220
Low tension	4	7.8971	0.5381
Low tension	5	10.1414	0.5575
Low tension	6	12.5296	0.5796
Low tension	7	15.0589	0.6037
Low tension	8	17.7743	0.6297
Low tension	9	20.6923	0.6574
Low tension	10	23.9318	0.6876
High tension	1	5.1400	1.5999
High tension	2	10.3000	1.6013
High tension	3	15.5000	1.6036
High tension	4	20.7000	1.6067
High tension	5	25.9000	1.6107

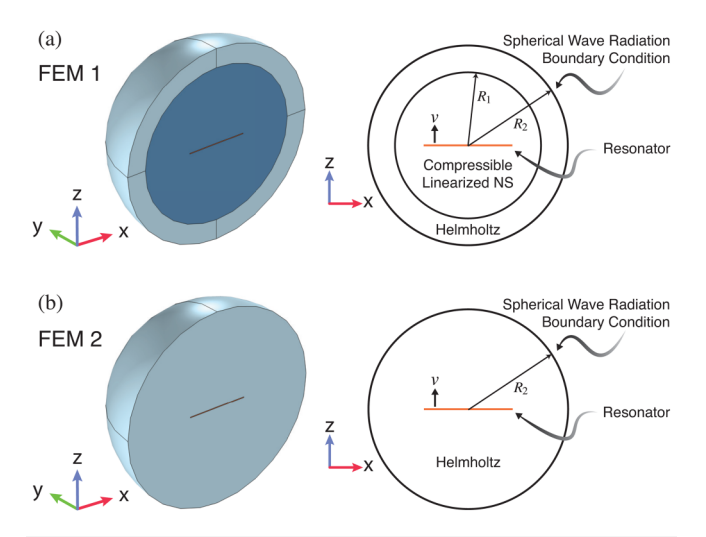


FIG. 2. Illustration of two 3D FEMs, FEM1 and FEM2, of resonator immersed in an infinite fluid medium. Fluid immediately surrounding the resonator is modeled with (a) compressible linearized NS equations in FEM1 and (b) Helmholtz equation in FEM2.

and will only include dissipation due to acoustic radiation. It will be shown that FEM1 offers the most accurate model of the physical problem, where the resonator is indeed vibrating in a viscous fluid. However, FEM2 will be used to compute the radiation efficiency of the resonator and estimate when acoustic radiation will be significant.

In both FEMs depicted in Fig. 2, only half of the resonator and spherical fluid domain are shown and analyzed due the symmetry about the x-z plane. The resonator is modeled identically in both models, with the length L, width b, and thickness h of the resonator taken to be about the x, y, and z axis, respectively. The resonator vibrates in the z-direction, and the resonator's velocity in the z-direction is denoted by ν , as depicted in Fig. 2. The two models differ in the governing equations used to model the fluid surrounding the resonator. FEM1, depicted in Fig. 2(a), models all linear fluidic dissipation mechanisms. Here, the fluid is modeled with two concentric spheres surrounding the resonator. The fluid domain within the sphere of radius R_1 is modeled with a Thermoviscous Acoustics solver to capture all the thermal and viscous losses that occur in the boundary layers. In this domain, the fluid is modeled as a viscous compressible Newtonian fluid with the compressible linearized NS equations. In the outer spherical layer between R_1 and R_2 , the fluid is modeled as a compressible lossless fluid and is governed by the Helmholtz equation. FEM2, depicted in Fig. 2(b), models the fluid as lossless and, therefore, only accounts for dissipation due to acoustic radiation. Here, the resonator is surrounded by a single sphere of fluid. In this domain, the fluid is modeled as a compressible lossless fluid and is governed by the Helmholtz equation. In both FEMs, the fluid is modeled as an infinite medium by imposing a spherical wave radiation boundary condition at the outer spherical boundary. This boundary condition

allows an outgoing spherical wave to leave the domain with minimal reflection. More details on the governing equations and boundary conditions may be found in the COMSOL Acoustics User's Manual.²⁵

To simulate the response of the microcantilever, the left end of the resonator is fixed, and an external harmonic force of frequency ω is applied to the right end. While keeping frequency constant, the mean background pressure p_0 , also referred to as the static ambient pressure, is swept. The mean background density of the gas is then computed with Eq. (7) using properties listed in Table II. The resonator is modeled to have dimensions listed in Table I with material properties of silicon:²⁶ elastic modulus $E = 170 \,\text{GPa}$ and density $\rho_s = 2329 \,\text{kg/m}^3$.

To simulate the response of the NEMS beams, the left and right ends of the resonator are fixed. The substrate is modeled in the FEMs by including a wall with a zero velocity boundary condition at a gap distance of $g=2\mu m$ away from the beam. The fluid is modeled with properties of air at atmospheric pressure listed in Table II. The resonator is modeled to have dimensions given in Sec. III B. Material properties found with the optimization search presented by Liem $et~al.,^{27}$ which minimizes the error between measured and predicted natural frequencies, are used in the FEMs. The free response of the NEMS beams is computed with an eigenfrequency analysis to find the natural frequencies and quality factors Q of the beam, as well as the mode shape of the beam and fluid.

For both the microcantilevers and NEMS beams, the resonators are modeled to have no material damping. Therefore, the computed dissipation is attributed to the losses in the gas.

B. Evaluating dissipation

With the evaluated FEMs, the dissipation for a forced response is evaluated with 28

$$\frac{1}{Q} = \frac{\overline{P}_{\text{dis}}}{\omega \overline{E}_{\text{stored}}},\tag{8}$$

where \overline{P}_{dis} is the time-averaged power dissipated and \overline{E}_{stored} is the time-averaged energy stored. As mentioned in Sec. IV, FEM1 and FEM2 differ in the governing equations of the near-field fluid. The total power dissipated in FEM1, which models the fluid with the compressible linearized NS equations, is

$$\overline{P}_{\rm dis} = \overline{P}_{\rm visc} + \overline{P}_{\rm therm} + \overline{P}_{\rm rad}, \tag{9}$$

where $\overline{P}_{\text{visc}}$ and $\overline{P}_{\text{therm}}$ are the time-averaged power dissipated due to viscous and thermal losses in the fluid, and $\overline{P}_{\text{rad}}$ is the time-averaged power radiated. The total dissipated power in FEM2, which models the fluid with the Helmholtz equation, is

$$\overline{P}_{\rm dis} = \overline{P}_{\rm rad}.\tag{10}$$

From Eq. (9), FEM1 accounts for viscous and thermal losses of the fluid, as well as the energy loss due to acoustic radiation. FEM2 models the fluid to be lossless, resulting in a dissipation that is only dependent on the energy loss due to acoustic radiation.

C. Evaluating radiation efficiency

To predict when acoustic radiation will be significant, the radiation efficiency 28 σ of a resonator is computed from

$$\sigma = \frac{\overline{P}_{\text{rad}}}{\rho_0 c S_s \langle \overline{v^2} \rangle},\tag{11}$$

where c is the speed of sound in the fluid, S_s is the area of the structural surface for which sound is radiated, and $\langle \overline{\nu^2} \rangle$ is the space-averaged value of the time-averaged squared vibrating velocity defined as

$$\langle \overline{v^2} \rangle = \frac{1}{S_s} \int_{S_s} \frac{1}{2} \operatorname{Re} \{ v v^* \} dS,$$
 (12)

where $(\cdot)^*$ indicates the complex-conjugate of the complex-valued argument. For the present work, the spatial average is taken about the top surface of the resonator, such that S_s is the surface area $L \times b$ of the resonator, and ν is the velocity in the z-direction at the resonator's top surface. The acoustic power radiated is computed from

$$\overline{P}_{\rm rad} = \int_{S_f} \overline{\mathbf{I}} \cdot \hat{\mathbf{n}} \ dS, \tag{13}$$

where $\hat{\boldsymbol{n}}$ is the unit normal vector and $\overline{\boldsymbol{I}}$ is the time-averaged intensity vector found from

$$\bar{\mathbf{I}} = \frac{1}{2} \operatorname{Re} \left\{ p \mathbf{u}_f^* \right\}, \tag{14}$$

where p is the acoustic pressure in the fluid and \mathbf{u}_f is the fluid velocity vector. Note that the acoustic pressure p is the pressure deviation from the ambient mean background pressure p_0 caused by sound waves. From Eq. (13), the power radiated is computed by integrating the dot product of the intensity vector and normal vector on the fluid surface S_f . For the present work, S_f is taken to be the outer spherical surface of the fluid domain. In the analyses that follow, the spherical surface is modeled at $R_2 = 3\lambda_{ac}$, where λ_{ac} is the acoustic wavelength in the fluid. Note that although the acoustic wave amplitude diminishes with radius, 29 the total power radiated remains constant due to the conservation of energy in the lossless fluid. Consequently, the power radiated evaluated with Eq. (13) is independent of the spherical surface, S_f .

The radiation efficiency in Eq. (11) characterizes the effectiveness of a vibrating surface to radiate sound. Small values of σ indicate that a relatively small amount of sound is radiated. By definition, a radiation efficiency of $\sigma=1$ indicates that the vibrating surface has the same efficiency as a circular baffled piston whose circumference greatly exceeds the acoustic wavelength. For the present work, the radiation efficiency in Eq. (11) is computed with results from FEM2, which models the fluid to be lossless. In this model, no energy is lost due to viscous or thermal losses, and all dissipation is due to acoustic radiation.

V. MEMS RESULTS

A. Measured normalized dissipation

The results from the experimental measurements discussed in Sec. III are plotted in Fig. 3. Here, all measurements are in the continuum viscous limit. This limit is based on the criteria presented in the work by Kara *et al.*²¹ Specifically, the measurements plotted are at pressures above the transition pressure p_c , which is dependent on the generalized Knudsen number Wi + Kn_l.

In Fig. 3, the measured dissipation, which was taken as a function of pressure, is normalized by the inverse of the mass loading parameter, T_0 , such that the plotted quantity is $1/(QT_0)$. The normalized dissipation is plotted against the dimensionless Reynolds number, which is related to the pressure dependent gas density ρ_0 by Eq. (3). This results in a collapse plot of normalized dissipation $1/(QT_0)$ vs Reynolds number α . The normalized dissipation predicted by the 2D viscous blade approximation is also plotted and is depicted by the black solid line. For the blade approximation, the normalized dissipation simplifies to $1/(QT_0) \approx \Gamma''_{\rm rect}$.

From Fig. 3, the viscous blade approximation accurately predicts the normalized dissipation for a few measurement sets. These measurements are depicted with gray markers and are seen to lie very near the black solid line. This indicates that dissipation is dominated by viscous losses in the fluid and acoustic radiation may be neglected, as the blade approximation models the fluid as incompressible. From Fig. 3, this is not true for all measurements, as deviation from the blade approximation is also observed. Measurements where the normalized dissipation differs from the blade approximation by more than 7.5% are indicated by the colored makers. For these measurements, the measured dissipation is larger than that predicted by the blade approximation, suggesting that additional energy is dissipated

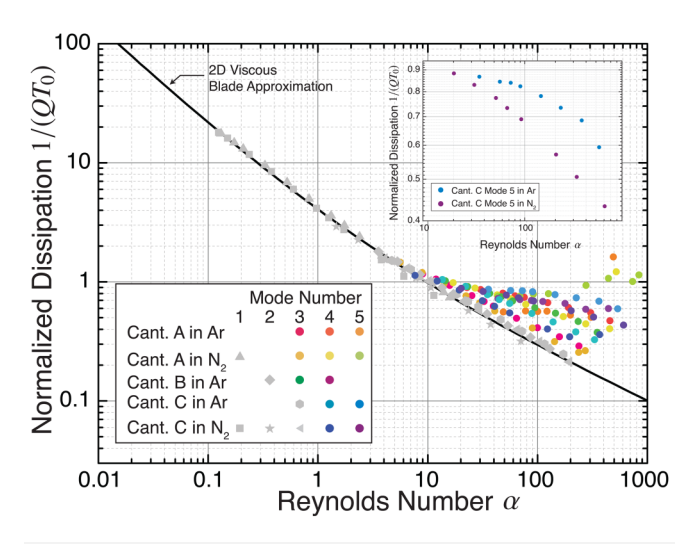


FIG. 3. Normalized dissipation, $1/(QT_0)$, vs Reynolds number α , for experimental measurements of microcantilevers in Ar and N₂. Measurements are compared to the normalized dissipation predicted by the blade approximation, where $1/(QT_0) \approx \Gamma''_{\text{rect}}$. Inset compares measurements for cantilever C vibrating in mode 5 in Ar and N₂.

due to a different physical mechanism. In Sec. V B, it will be shown that these measurements are taken from resonators with a relatively large radiation efficiency σ , suggesting that the additional dissipation is due to acoustic radiation.

B. Computed radiation efficiency

The radiation efficiency σ computed from Eq. (11) with FEM2 discussed in Sec. IV is plotted in Fig. 4. The radiation efficiency was computed for each resonator and frequency listed in Table III at a mean background pressure of $p_0=101$ 325Pa. In Fig. 4, the radiation efficiency is plotted vs the wavenumber ratio κ defined as

$$\kappa = \frac{k_{ac}}{k_b},\tag{15}$$

where k_{ac} is the acoustic wavenumber defined as

$$k_{ac} = \frac{\omega}{c},\tag{16}$$

where ω is the angular frequency and c is the speed of the sound in the fluid. In Eq. (15), k_b is the bending wavenumber defined as

$$k_b = \left(\frac{\rho_s A \omega^2}{EI}\right)^{1/4},\tag{17}$$

where A is the cross-sectional area and I is the moment of inertia of the beam's cross section. A wavenumber k is also related to the wavelength λ by

$$k = \frac{2\pi}{\lambda}. (18)$$

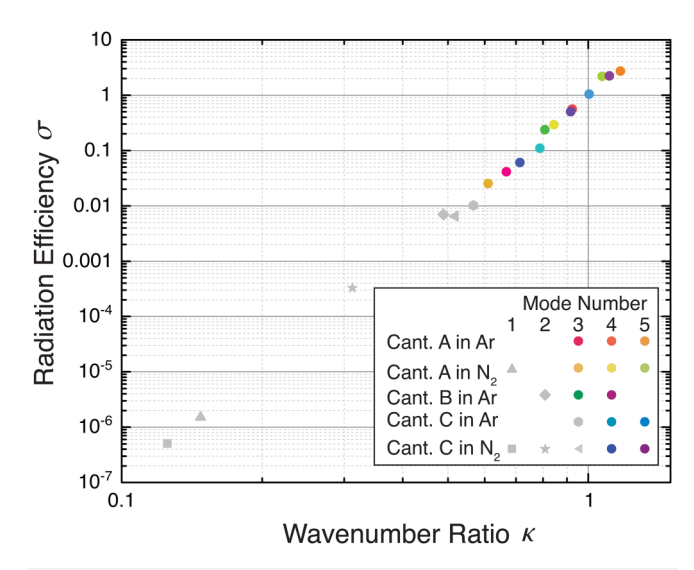


FIG. 4. Radiation efficiency σ plotted vs wavenumber ratio κ for the measured microcantilevers.

TABLE V. Acoustic wavenumber, bending wavenumber, and wavenumber ratio for measured microcantilevers

		Mode 1			Mode 2			Mode 3			Mode 4			Mode 5	
	$k_{ac} k_b (1/\mu m) (1/\mu m)$	k_b $(1/\mu\mathrm{m})$	K	k_{ac} $(1/\mu \mathrm{m})$	k_b (1/ μ m)	K	k_{ac} $(1/\mu \mathrm{m})$	k_b $(1/\mu\mathrm{m})$	K	k_{ac} $(1/\mu \mathrm{m})$	k_b $(1/\mu \mathrm{m})$	K	k_{ac} (1/ μ m)	k_b (1/ μ m)	K
Cant. A in Ar							0.0480	0.0720	0.66763	0.0920	0.0996	0.924 11	0.1481	0.1264	1.17230
Cant. A in N2	0.0026	0.0174 0.147 76	0.147 76				0.0439	0.0719	0.61009	0.0841	0.0996	0.84438	0.1354	0.1264	1.0715
Cant. B in Ar				0.0258	0.0528	0.48954	0.0702	0.0870	0.80705	0.1327	0.1196	1.10960			
Cant. C in Ar							0.0347	0.0612	0.5675	0.0669	0.0849	0.78789	0.1087	0.1082	1.00410
Cant. C in N2 0.0019 0.0148 0.125 40	0.0019	0.0148	0.12540	0.0115	0.0368	0.31210	0.0317	0.0612	0.51866	0.0611	0.0849	0.714 05	0.0992	0.0849	0.91735

From Eq. (18), the wavenumber ratio κ is also related to the acoustic and bending wavelength, λ_{ac} and λ_b , respectively, by

$$\kappa = \frac{\lambda_b}{\lambda_{ac}}. (19)$$

The acoustic wavenumber, bending wavenumber, and wavenumber ratio for the measured microcantilevers are listed in Table V.

From Fig. 4, the measurements that agreed well with the viscous blade approximation correspond to a low radiation efficiency. This supports the previous claim that acoustic radiation is negligible for these measurements, and the dissipation may be accurately predicted by only considering viscous losses. Furthermore, results in Figs. 3 and 4 show that measurements that disagree with the blade approximation have a relatively large radiation efficiency. For these measurements, the vibration of the microcantilever resulted in radiated sound, and consequently an observed increase in dissipation.

An increase in radiation efficiency σ with increase in ratio of wavenumbers κ is observed in Fig. 4. From Eq. (19), when κ is less than unity, the acoustic wavelength in the fluid is greater than the bending wavelength, such that $\lambda_{ac} > \lambda_b$. For small values of κ , the microcantilever is unable to radiate a significant amount of sound and the radiation efficiency σ is relatively small. However, as κ increases and the bending wavelength approaches the length of the acoustic wavelength, the radiation efficiency increases. This increase in radiation efficiency corresponds to an increase in acoustic power radiated, as predicted by Eq. (11), attributed to pressure waves generated by the vibrating microcantilever. From analyses presented by Fahy and Gardonio²⁸ the radiation efficiency is maximum near a wavenumber ratio equal to unity. Specifically, Fahy et al. computed the radiation efficiency of a vibrating plate and showed that the radiation efficiency increases as the wavenumber ratio increases and approaches unity. Additionally, they showed that the radiation efficiency is at a maximum when the wave number ratio is slightly greater than unity, and asymptotes for large wavenumber ratios. Note that a wavenumber ratio of $\kappa \approx 1$ corresponds to $\lambda_{ac} \approx \lambda_b$. Although results in Fig. 4 correspond to relatively small wavenumber ratios and a well defined maximum is not observed, the results follow the general trends presented by Fahy et al..28 In particular, the radiation efficiency increases as the wavenumber ratio increases and approaches unity.

To further interpret the results in Figs. 3 and 4, Fig. 5 illustrates how pressure fields depend on the wavenumber ratio κ . Specifically, Fig. 5 plots results from FEM2 that simulated cantilever B in Ar at $p_0=101\,325\,\mathrm{Pa}$. Results from a simulation that excited the second mode at $\omega/2\pi=1.311\,\mathrm{MHz}$ and fourth mode at $\omega/2\pi=6.738\,\mathrm{MHz}$, are plotted in Figs. 5(a) and 5(b), respectively. For both simulations, the spherical fluid domain was set to $R_2=3\lambda_{ac}$, where the acoustic wavelength in the fluid, $\lambda_{ac}=2\pi c/\omega$, varied between simulations due to the varying frequencies. In Fig. 5, color on the outer spherical surface of the 3D plot represents the normalized intensity magnitude $\|\mathbf{I}\|/\left(\rho_0 c S_s \langle \overline{v^2} \rangle\right)$. The isosurfaces in the 3D plot and color in the 2D plot represent normalized acoustic pressure, $\mathrm{Re}\{p\}/\left(\rho_0 c S_s \langle \overline{v^2} \rangle\right)$. Recall that acoustic

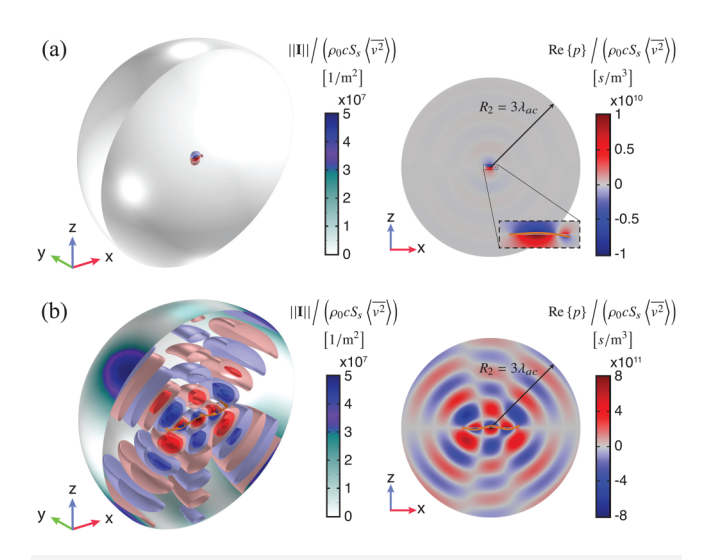


FIG. 5. Results from 3D FEM which simulated cantilever B in Ar at $\rho_0=101\,325\,\text{Pa}$ vibrating in its (a) second and (b) fourth mode. Color on outer spherical surface of 3D plot represents normalized intensity magnitude $\left\|\mathbf{II}\right\| \left/ \left(\rho_0 c S_s \left\langle \overline{v^2} \right\rangle \right).$ Isosurfaces in 3D plot and color in 2D plot represent normalized acoustic pressure, Re{ $\rho \} \left/ \left(\rho_0 c S_s \left\langle \overline{v^2} \right\rangle \right).$

pressure is the deviation from the mean background pressure caused by the generated sound wave. The 2D plot is of the x-z plane taken at the middle of the microcantilever width.

From Table V, the wavenumber ratio κ for cantilever B vibrating in Ar is 0.48954 and 1.10960 for modes 2 and 4, respectively. Additionally, the radiation efficiency for modes 2 and 4 is $6.733\times10^{\dot{-}3}$ and 2.152, respectively, suggesting that mode 4 radiates more sound than mode 2. This is observed in Fig. 5, where the normalized intensity magnitude for mode 2 is significantly less than that for mode 4. From Eq. (13), a relatively large intensity results in a relatively large power radiated and thus a greater amount of energy dissipated. The observed difference in intensity between modes 2 and 4 is due to the difference in generated pressure fields. From Fig. 5(a), when the microcantilever vibrates in its second mode, the pressure field is mostly localized to the field close to the vibrating surface. This is due to the fact that the acoustic wavelength in the fluid λ_{ac} is much larger than the bending wavelength λ_b . In contrast, when the microcantilever vibrates in its fourth mode, the wavenumber ratio is greater than unity and $\lambda_b > \lambda_{ac}$. From Fig. 5(b), the vibrating microcantilever generates pressure waves that radiate throughout the fluid.

When the bending wavelength is comparable to the acoustic wavelength, the vibrating microcantilever efficiently radiates sound. This is evident by the results presented in Figs. 4 and 5. Furthermore, an increase in acoustic radiation gives rise to an increase in dissipation. In the inset of Fig. 3, the normalized dissipation for cantilever C vibrating in mode 5 in Ar and N_2 is plotted. Although the measurements were taken for the same cantilever vibrating in the same mode, the normalized dissipation's dependence on Reynold's number varied between gases. This is due to the difference in the speed of sound in

Ar and N_2 , and consequently the difference in the acoustic wavelength and wavenumber ratio. From Table II, the sound speed in Ar is less than that in N_2 , resulting in a smaller acoustic wavelength, and larger wavenumber ratio. From Fig. 4, this gives rise to a larger radiation efficiency and thus an increase in acoustic radiation and dissipation, as observed in Fig. 3. From Fig. 3, when acoustic radiation is significant, the dissipation may no longer be predicted by the viscous blade approximation. Additionally, the dissipation is no longer solely dependent on the Reynolds number α , but also dependent on the acoustic and bending wavelengths.

C. Computed dissipation

To observe the dissipation's dependence on the ambient mean background pressure p_0 , the measured dissipation 1/Q for cantilever C in N2 is plotted in Fig. 6 for each measured mode. The dissipation is plotted vs the mean background pressure p_0 of the gas. Here, all measurements, including those in the kinetic regime are plotted. The kinetic and continuum regimes are indicated by the blue and red shaded regions respectively. The transition pressure defined by Kara et al. 21 is also depicted with the vertical dashed line. Here, the transition pressure was computed by finding the generalized Knudsen number Wi + Kn_l \approx 1. In Fig. 6, the measured dissipation is compared to the dissipation computed from FEM1 at pressures above the transition pressure. Recall that FEM1 solves the compressible linearized NS equations and accounts for all the losses in the fluid. Additionally, the measurements are compared to the dissipation predicted by the viscous blade approximation and Eq. (5).

From Fig. 6, the dissipation predicted by FEM1 agrees well with the data in the continuum regime for every mode. This is due to the fact that FEM1 accounts for all the losses in the system, namely, viscous and thermal losses of the fluid and any acoustic radiation. As previously observed, the blade approximation accurately predicts the dissipation for modes 1–3, where the wavenumber ratio is relatively small. At these frequencies, dissipation due to acoustic radiation may be neglected. However, for modes 4 and 5, disagreement between the measured and predicted dissipation is observed. Here, the blade approximation underpredicts the dissipation by not accounting for compressibility of the fluid and thus any acoustic radiation.

The presence of acoustic radiation is also evident by the pressure dependence of the dissipation. In the kinetic regime, dissipation depends linearly with ambient pressure, such that $1/Q \propto p_0$. In the continuum regime, the physical dissipation mechanism changes, giving rise to a change in pressure dependence and slope of the dissipation curve. For modes 1-3, where acoustic radiation is negligible, the slope in the dissipation curves for data, FEM1, and blade approximation are very similar. For these modes, the dissipation is dominated by viscous losses in the continuum regime. Beginning at mode 4, the slope in the dissipation curves for data and FEM1 begins to differ from that of the blade approximation in the continuum regime. This is best observed in mode 5, where the slope of the data and FEM1 dissipation curves is noticeably larger than that of the blade approximation. This change in pressure dependence is due to the additional losses attributed to acoustic radiation. As viscous dissipation and acoustic radiation

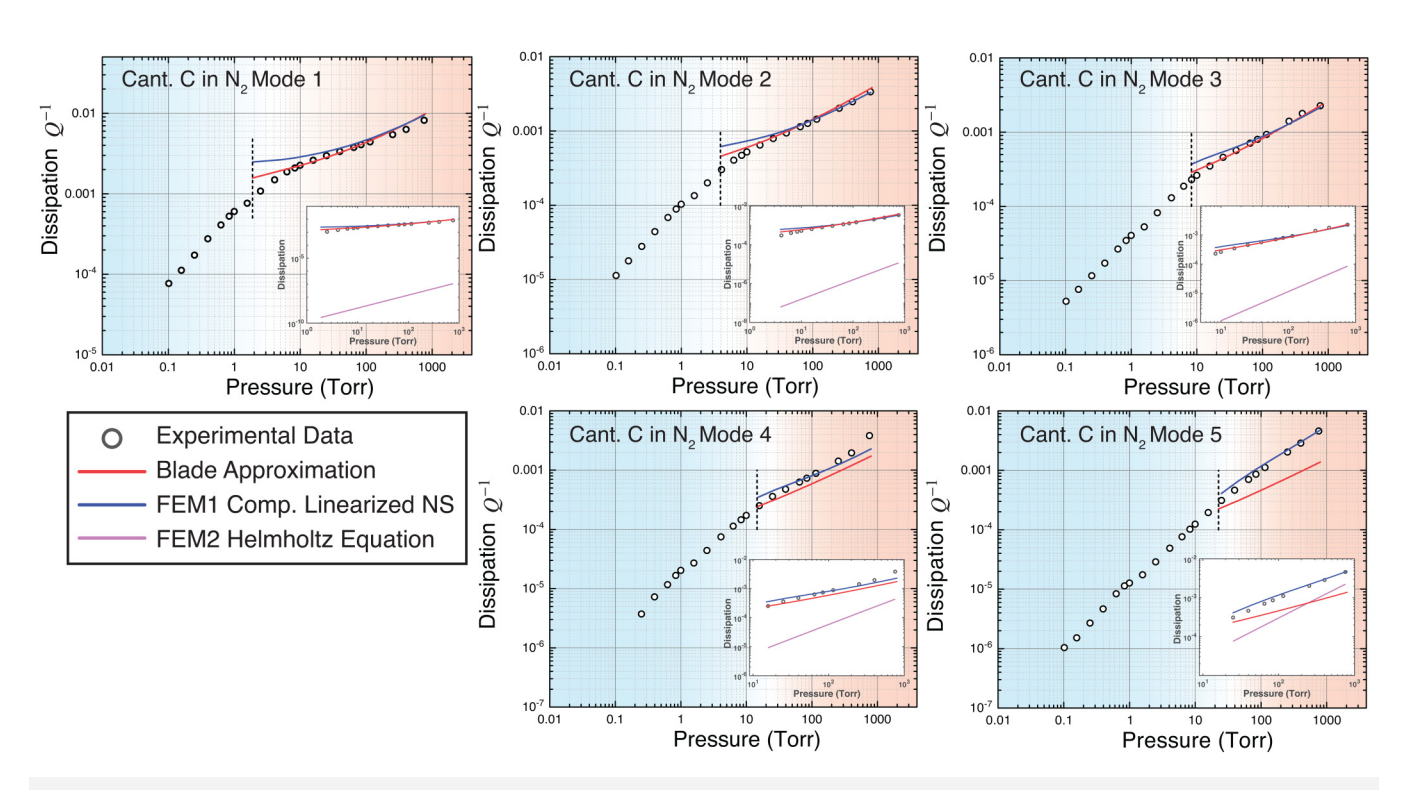


FIG. 6. Dissipation 1/Q plotted vs mean background pressure p_0 for cantilever C in N_2 for modes 1–5. Vertical dashed line indicates transition pressure from kinetic regime to continuum regime. Inset compares measured dissipation to dissipation predicted by blade approximation, FEM1, and FEM2 at pressures above transition pressure.

have different pressure dependencies, the change in slope represents a transition from dissipation dominated by viscous losses, to that which also has acoustic radiation. Results from Fig. 6 may be better interpreted by analyzing dissipation for two canonical models.

Here, we consider the dissipation of a vibrating piston in an infinite lossless fluid and an oscillating cylinder in a viscous incompressible fluid. The former dissipates energy due to acoustic radiation, whereas the latter dissipates energy due to viscous losses. It is important to note that the two canonical models vary drastically in geometry and make different simplifications to the fluid, resulting in very different quality factors. However, in the following results, we are primarily focused on comparing the asymptotic behavior of the two dissipation models. Figure 7 plots the dissipation 1/Q vs mean background pressure p_0 predicted from two the two canonical models. The first model is of a vibrating piston in an infinite lossless fluid. The 1D plane waves generated by the oscillating piston result in energy loss due to acoustic radiation, as no waves are reflected back. For this model, the fluid is considered to be inviscid, resulting in no dissipation due to viscous losses. From Eq. (9), the dissipation due to acoustic radiation of an oscillating piston is

$$\frac{1}{Q_{\rm ac}} = \frac{\rho_0 c}{\omega \rho_s d},\tag{20}$$

where ρ_s is the density of the piston, and d is the linear dimension of the piston in the direction of oscillation. The second model is of a solid cylinder oscillating in a viscous incompressible fluid. In this model, the dissipation is due to viscous losses in the fluid and is

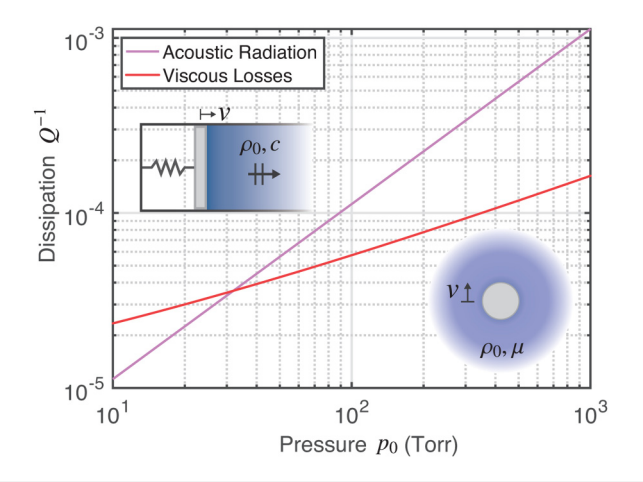


FIG. 7. Dissipation 1/Q plotted vs pressure p_0 for a piston vibrating in an infinite lossless fluid, and a cylinder oscillating in an infinite incompressible viscous fluid.

$$\frac{1}{Q_{\text{visc}}} = \frac{\rho_0 \Gamma_{\text{circ}}^{"}(\alpha)}{\rho_s},$$
(21)

where ρ_s is the density of the cylinder. From Sec. II, α is the Reynolds number defined in Eq. (3) and Γ''_{circ} is the imaginary part of the hydrodynamic function defined in Eq. (2).

The dissipation predicted in Eqs. (20) and (21) is plotted in Fig. 7 vs mean background pressure p_0 . The frequency of oscillation was taken to be $\omega/2\pi = 1 \,\mathrm{MHz}$, the density of the solid was $\rho_s = 2$, 329 kg/m³, and the linear dimension of the piston and the diameter of the cylinder was taken to be $d = 32.5 \,\mu\text{m}$. The fluid was taken to be N2. Based on the frequency of oscillation and linear dimension, the pressure range plotted in Fig. 7 is above the transition pressure. Here, the results plotted are in the continuum limit such that the generalized Knudsen number is Wi + Kn $_l \ll 1$. From Eq. (20), the dissipation due to acoustic radiation varies with the pressure dependent gas density ρ_0 . From Eq. (7), density depends linearly with pressure. Consequently, the dissipation in Eq. (20) depends linearly with pressure, such that $1/Q \propto p_0$. This is observed in Fig. 7, where dissipation vs pressure is plotted in log-log, and the resulting curve has a slope of $m_{ac} = 1$. From Eq. (21), the dissipation due to viscous losses of an oscillating cylinder is more complex. Here, dissipation varies linearly with $\rho_0 \Gamma''_{circ}(\alpha)$, where the hydrodynamic function is computed from Bessel functions in Eq. (2) with the pressure dependent Reynolds number α . This gives rise to the approximate pressure dependence^{21,30} of $1/Q \propto p_0^{1/2}$, which is reflected in Fig. 7 through the smaller slope of the viscous dissipation curve.

Observing Fig. 6 again, a clear change in slope for data in the kinetic and continuum regime is observed for modes 1–3, as dissipation is dominated by viscous losses in the continuum regime. Consequently, the dissipation's pressure dependence changes from $1/Q \propto p_0$ to $1/Q \propto p_0^{1/2}$, when changing from the kinetic to continuum regime. In contrast, the slope change in modes 4 and 5 is more subtle. This is due to the presence of acoustic radiation and the resulting increase in slope in the continuum regime. The increase in slope suggests that acoustic radiation contributes to the total measured dissipation, which is no longer dominated by viscous losses.

The dissipation predicted by FEM2, which solved the Helmholtz equation, may also be observed in the inset of each plot. The inset plots the measured dissipation, and the dissipation predicted by the blade approximation, FEM1, and FEM2 for pressures above the transition pressure. In general, when the fluid is modeled to be lossless, as in FEM2, the predicted dissipation greatly underpredicts the measured dissipation because it does not account for any viscous losses. The largest disagreement between data and FEM2 occurs at the first mode, where the viscous boundary layer is relatively large due to the low frequency, resulting in relatively large viscous losses. Furthermore, the acoustic radiation is small due to the large acoustic wavelength. In contrast, it is observed that the difference between measured and predicted dissipation from FEM2 is smaller for mode 5. This decrease in disagreement is due to the decrease in viscous losses and the increase in acoustic radiation. The results from FEM2 show that dissipation attributed to acoustic radiation increases with mode number due to the resulting decrease in acoustic wavelength in the fluid and increase in wavenumber ratio.

VI. NEMS RESULTS

In Fig. 8, the measured normalized dissipation $1/(QT_0)$ for each mode of the low tension and high tension doubly clamped NEMS beam is plotted vs Reynolds number α . Here, the Reynolds number in Eq. (3) varies due to the change in frequency at each mode. The measured dissipation is compared to the predicted dissipation from FEM2, which solves the Helmholtz equation. Recalling Sec. IV, FEM2 modeled the fluid to be compressible and inviscid, resulting in dissipation solely attributed to acoustic radiation. In Fig. 8, the normalized dissipation predicted by the 2D viscous blade approximation is also plotted and is depicted by the solid black line. We note that the generalized Knudsen number for all the beams remain below 1, Kn + Wi < 1. However, especially for the high frequency modes, the flow may not be fully continuum, necessitating the incorporation of a slip boundary condition³¹ for a more accurate description. Regardless, the close agreement between experiment and continuum theory indicates that the rarefaction effects may be ignored.

From Fig. 8, the dissipation predicted by FEM2 underpredicts the measured dissipation. While the acoustic wave equation may need small corrections for the high frequency modes of these devices due to rarefaction in the gas, ³² our results show the main trends. These results imply that the measurements have a significant amount of viscous dissipation, which is not accounted for in the numerical model. Instead, the dissipation predicted by FEM2 only computes losses due to acoustic radiation. Consequently, the results in Fig. 8 indicate that acoustic radiation increases with an increase in mode number. The dissipation due to acoustic radiation is observed to increase by four orders of magnitude from mode 1 to mode 10 for the low tension beam, and three orders of

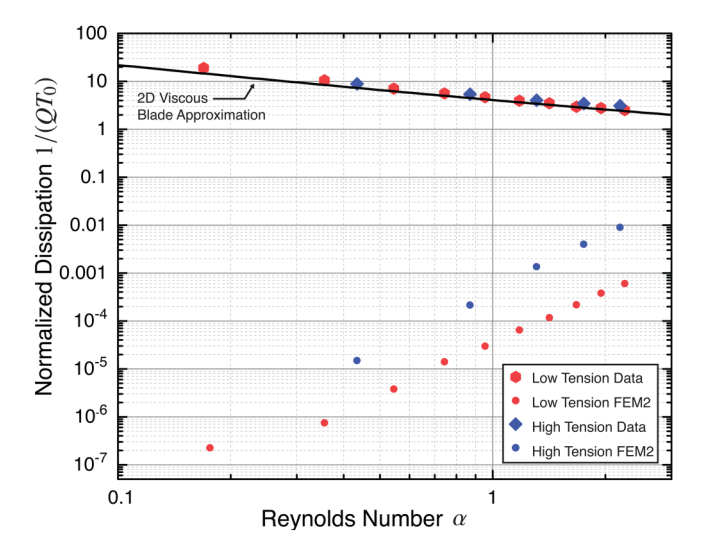
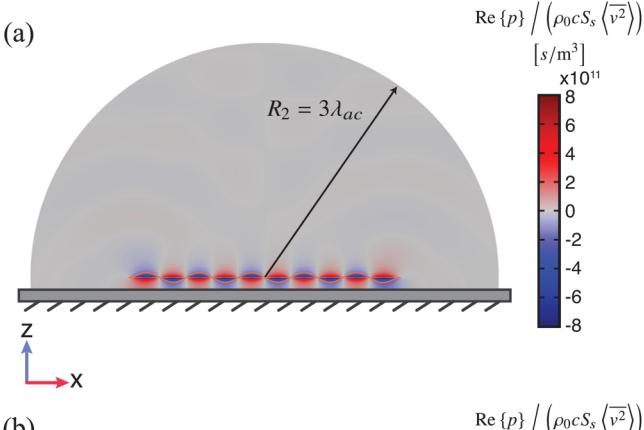


FIG. 8. Normalized dissipation, $1/(QT_0)$, vs Reynolds number α for experimental measurements of doubly clamped NEMS beams with tension in air at atmospheric pressure. Measurements are compared to numerical predication from FEM2, and the normalized dissipation predicted by the blade approximation, where $1/(QT_0) \approx \Gamma_{\rm rect}^{\prime\prime}$.

magnitude from mode 1 to mode 5 for the high tension beam. This increase is due to the decrease in acoustic wavelength in the fluid, and resulting increase in wavenumber ratio. The wavenumber ratios for the low tension and high tension beams are listed in Table IV. Note that the expression for the bending wavenumber for a beam with axial loading is different from that expressed in Eq. (17). Particularly, the wavenumber of the propagating bending wave is different in magnitude than that of the evanescent bending wave.³³ The wavenumber ratios listed in Table IV are evaluated with Eq. (15) and the computed bending wavenumber for the forward propagating bending wave. Expressions for the bending wavenumber for a beam with axial loading may be found in the work by Bokaian.³³

From Fig. 8, it is observed that the high tension beam radiates more sound than the low tension beam. Specifically, the numerically predicted dissipation for mode 5 of the high tension beam is larger than that for mode 10 of the Low Tension beam. Although the two modes have similar Reynolds number and, therefore, similar natural frequencies, a considerable difference in dissipation is observed. This observation may be better interpreted with Fig. 9, which plots the normalized acoustic pressure field, Re{ p}/ $(\rho_0 c S_s \langle \overline{v^2} \rangle)$, for mode 10 of the low tension beam and mode 5 of the high tension



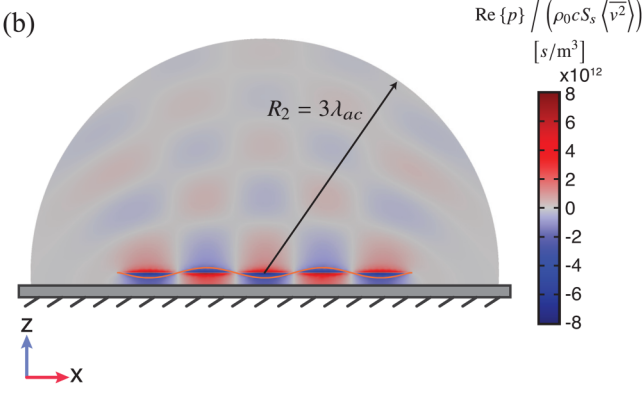


FIG. 9. Normalized acoustic pressure, Re{ p}/ $\left(\rho_0 c S_s \langle \overline{v^2} \rangle\right)$, plotted in x-z plane for (a) mode 10 of low tension beam and (b) mode 5 of high tension beam.

beam. The pressure field is plotted in the x-z plane taken at the middle of the beam width. Comparing Figs. 9(a) and 9(b), it is clear that the high tension beam radiates more sound resulting in larger dissipation due to acoustic radiation. In contrast to the high tension beam, which generates pressure waves throughout the fluid, vibration of the low tension beam results in localized pressure fields. Although the high tension beam radiates more sound than the low tension beam, it is important to note that both beams follow the same trend of an increase in acoustic radiation with increase in mode number and thus wavenumber ratio.

VII. RADIATION OF ARBITRARY RESONATING BEAMS

From the results presented in Secs. V and VI, acoustic radiation becomes prominent when the bending wavelength approaches the length of the acoustic wavelength. Furthermore, when the acoustic wavelength is much larger than the bending wavelength such that κ is relatively small, acoustic radiation is negligible and viscous dissipation dominates. Substituting the expressions for the acoustic and bending wavenumber in Eqs. (16) and (17), respectively, into Eq. (15), results in the following expression for wavenumber ratio:

$$\kappa = \left(\frac{\omega}{c}\right) \left(\frac{Eh^2}{12\rho_c \omega^2}\right)^{1/4}.$$
 (22)

With Eq. (22), one may estimate if acoustic radiation will be negligible by computing the wavenumber ratio for a given frequency of oscillation ω , and properties of the beam and fluid. Furthermore, Eq. (22) may be used as a tool when designing miniaturized resonators when in the continuum limit. As most resonators are driven at resonance to excite a bending mode, it is helpful to consider the nth natural frequency of a beam

$$\omega_n = \left(\frac{k_{b,n}^4 EI}{\rho A}\right)^{1/2},\tag{23}$$

where $k_{b,n}$ are the discrete modal bending wavenumbers given by

$$k_{b,n} = \frac{\beta_n}{I},\tag{24}$$

and β_n are the normalized modal bending wavenumbers that satisfy the characteristic frequency equation for the boundary conditions of the beam. Values of β_n for a beam with fixed-free (cantilever) and fixed-fixed boundary conditions are listed in Table VI. Substituting the expression for the discrete natural frequencies of a beam in Eq. (24) into Eq. (22) and simplifying results in

$$\kappa_n = \frac{\beta_n}{\sqrt{12}} \left(\frac{h}{L}\right) \left(\frac{c_s}{c}\right),\tag{25}$$

where c_s is the longitudinal sound speed in a bar given by

$$c_s = \sqrt{\frac{E}{\rho_s}}. (26)$$

TABLE VI. Normalized dimensionless modal bending wavenumbers for fixed–free and fixed–fixed beams.

	No	rmalized	bending w	avenumbe	$r \beta_n$
	Mode 1	Mode 2	Mode 3	Mode 4	Mode 5
Fixed-free	1.8749	4.6941	7.8548	10.9955	14.1372
Fixed-fixed	4.7300	7.8532	10.9956	14.1372	17.2788

From Eq. (25), the wavenumber ratio for a bending mode κ_n depends on the thickness to length aspect ratio h/L and ratio of the longitudinal sound speed in the solid to the speed of sound in the fluid c_s/c . This implies that miniaturized resonators with small linear dimensions, such as MEMS and NEMS resonators, may radiate sound provided that the aspect ratio gives rise to a wavenumber ratio $\kappa \approx 1$. Furthermore, the expression in Eq. (25) shows that the wavenumber ratio increases with increasing mode number due to the increase in β_n with mode number. This increases is implicitly due to the frequency dependencies of the acoustic and bending wavelengths. Since the acoustic wavelength depends on frequency with $\lambda_{ac} \propto 1/\omega$, and the bending wavelength depends on frequency with $\lambda_b \propto 1/\sqrt{\omega}$, the wavenumber ratio in Eq. (19) increases with frequency and thus mode number. From Eq. (26) and observed in the results in Secs. V and VI, although κ may be small for lower modes, it quickly increases with mode number, giving rise to an increase in acoustic radiation. If a high quality factor Q resonator is desired, one should design a resonator with a small thickness to length aspect ratio, h/L, to limit the dissipation due to acoustic radiation.

VIII. CONCLUSION

Measurements from microcantilevers and NEMS beams are presented and show an increase in dissipation due to acoustic radiation. Numerical simulations show that the increase in acoustic radiation is due to an increase in radiation efficiency, which is dependent on the ratio of acoustic wavelength in the fluid to bending wavelength. When the bending wavelength is comparable to the acoustic wavelength, acoustic radiation becomes prominent and the 2D viscous approximations can no longer accurately predict the total dissipation. Due to the frequency dependence of the acoustic and bending wavelength, the wavenumber ratio will increase with increasing mode number. To limit the amount of dissipation due to acoustic radiation, resonators should be designed with small thickness to length aspect ratios in order to decrease the wavenumber ratio. Results presented here also give insight and design guidance beyond dissipation effects. If, instead, acoustic radiation is desired for the sensing of resonators, one would design resonators such that the wavenumber ratio would be near unity.

More research is needed for developing an appropriate acoustic wave equation applicable to small and high frequency devices. Navier–Stokes equations have been shown to break down both at the limit when the mean free path or the relaxation time in the fluid

becomes large. ²¹ Similar considerations should emerge when describing acoustic radiation from small and high frequency oscillators.

ACKNOWLEDGMENTS

This material is based on the work supported by the National Science Foundation Graduate Research Fellowship Program (Grant No. DGE-1840990). Partial support from the National Science Foundation (NSF) (Grant Nos. CBET-1604075 and CMMI-2001403) is also acknowledged. Any opinions, findings, and conclusions or recommendations expressed in this material are those of the authors and do not necessarily reflect the views of the National Science Foundation.

DATA AVAILABILITY

The data that support the findings of this study are available within the article.

REFERENCES

¹M. Calleja, P. M. Kosaka, Á. San Paulo, and J. Tamayo, "Challenges for nano-mechanical sensors in biological detection," Nanoscale 4, 4925–4938 (2012).

²M. Li, E. B. Myers, H. X. Tang, S. J. Aldridge, H. C. McCaig, J. J. Whiting, R. J. Simonson, N. S. Lewis, and M. L. Roukes, "Nanoelectromechanical resonator arrays for ultrafast, gas-phase chromatographic chemical analysis," Nano Lett. 10, 3899–3903 (2010).

³C. Lissandrello, F. Inci, M. Francom, M. R. Paul, U. Demirci, and K. L. Ekinci, "Nanomechanical motion of *Escherichia coli* adhered to a surface," Appl. Phys. Lett. **105**, 113701 (2014).

⁴O. Svitelskiy, V. Sauer, N. Liu, K.-M. Cheng, E. Finley, M. R. Freeman, and W. K. Hiebert, "Pressurized fluid damping of nanoelectromechanical systems," Phys. Rev. Lett. **103**, 244501 (2009).

 5 C. Lissandrello, L. Li, K. L. Ekinci, and V. Yakhot, "Noisy transitional flows in imperfect channels," J. Fluid. Mech. 778, 0 (2015).

⁶J. E. Sader, "Frequency response of cantilever beams immersed in viscous fluids with applications to the atomic force microscope," J. Appl. Phys. **84**, 64-76 (1998).

⁷G. G. Stokes, "On the effect of the internal friction of fluids on the motion of pendulums," Trans. Cambridge Philos. Soc. **9**, 8–106 (1851). ⁸J. W. M. Chon, P. Mulvaney, and J. E. Sader, "Experimental validation of theo-

⁸J. W. M. Chon, P. Mulvaney, and J. E. Sader, "Experimental validation of theoretical models for the frequency response of atomic force microscope cantilever beams immersed in fluids," J. Appl. Phys. 87, 3978–3988 (2000).

⁹C. Yu-Hang and H. Wen-Hao, "Resonant response of rectangular AFM cantilever in liquid," Chin. Phys. Lett. **24**, 363–365 (2007).

¹⁰C. Lissandrello, V. Yakhot, and K. L. Ekinci, "Crossover from hydrodynamics to the kinetic regime in confined nanoflows," Phys. Rev. Lett. 108, 084501 (2012).

¹¹S. Basak, A. Raman, and S. V. Garimella, "Hydrodynamic loading of micro-cantilevers vibrating in viscous fluids," J. Appl. Phys. 99, 114906 (2006).

¹²A. Maali, T. Cohen-Bouhacina, C. Jai, C. Hurth, R. Boisgard, J. P. Aimé, D. Mariolle, and F. Bertin, "Reduction of the cantilever hydrodynamic damping near a surface by ion-beam milling," J. Appl. Phys. 99, 024908 (2006).

¹³A. T. Liem, A. B. Ari, C. Ti, M. J. Cops, J. G. McDaniel, and K. L. Ekinci, "Nanoflows induced by MEMS and NEMS: Limits of two-dimensional models," Phys. Rev. Fluids 6(2), 024201 (2021).

¹⁴R. M. Lin and W. J. Wang, "Structural dynamics of microsystems—Current state of research and future directions," Mech. Syst. Signal Process. 20, 1015–1043 (2006).

¹⁵S. D. Vishwakarma, A. K. Pandey, J. M. Parpia, D. R. Southworth, H. G. Craighead, and R. Pratap, "Evaluation of mode dependent fluid damping in a high frequency drumhead microresonator," J. Microelectromech. Syst. 23, 334–346 (2014).

- 16E. Gil-Santos, C. Baker, D. T. Nguyen, W. Hease, C. Gomez, A. Lemaître, S. Ducci, G. Leo, and I. Favero, "High-frequency nano-optomechanical disk resonators in liquids," Nat. Nanotechnol. 10, 810-816 (2015).
- 17M. R. Paul, M. T. Clark, and M. C. Cross, "Coupled motion of microscale and nanoscale elastic objects in a viscous fluid," Phys. Rev. E 88, 043012 (2013).

 18 L. Rosenhead, *Laminar Boundary Layers* (Clarendon Press, Oxford, 1963).
- $^{\mathbf{19}}\text{S. S.}$ Chen, M. W. Wambsganss, and J. A. Jendrzejczyk, "Added mass and damping of a vibrating rod in confined viscous fluids," J. Appl. Mech. 43, 325-329 (1976).
- ²⁰M. R. Paul, M. T. Clark, and M. C. Cross, "The stochastic dynamics of micron and nanoscale elastic cantilevers in fluid: Fluctuations from dissipation," Nanotechnology 17, 4502-4513 (2006).
- ²¹V. Kara, V. Yakhot, and K. L. Ekinci, "Generalized Knudsen number for unsteady fluid flow," Phys. Rev. Lett. 118, 074505 (2017).
- ²²N. M. M. Maia and J. M. M. Silva, Theoretical and Experimental Modal Analysis (Research Studies Press, 1997).
- ²³A. B. Arı, M. Çağatay Karakan, C. Yanık, I. I. Kaya, and M. Selim Hanay, "Intermodal coupling as a probe for detecting nanomechanical modes," Phys. Rev. Appl. 9, 034024 (2018).
- ²⁴COMSOL Multiphysics v.5.4, COMSOL AB, Stockholm, Sweden, see www. comsol.com.

- 25 Acoustics Module User's Guide, COMSOL Multiphysics v.5.4, COMSOL AB, Stockholm, Sweden (2018).
- ²⁶M. A. Hopcroft, W. D. Nix, and T. W. Kenny, "What is the Young's modulus of silicon?," J. Microelectromech. Syst. 19, 229-238 (2010).
- ²⁷A. T. Liem, A. B. Ari, J. G. McDaniel, and K. L. Ekinci, "An inverse method to predict NEMS beam properties from natural frequencies," J. Appl. Mech. 87, 4046445 (2020).
- 28 F. J. Fahy and P. Gardonio, Sound and Structural Vibration (Academic Press,
- ²⁹D. T. Blackstock, Fundamentals of Physical Acoustics (John Wiley & Sons,
- 30 D. M. Karabacak, V. Yakhot, and K. L. Ekinci, "High-frequency nanofluidics: An experimental study using nanomechanical resonators," Phys. Rev. Lett. 98, 254505 (2007).
- 31 E. Lauga, M. Brenner, and H. Stone, "Microfluidics: The no-slip boundary condition," in Springer Handbook of Experimental Fluid Mechanics, edited by C. Tropea, A. L. Yarin, and J. F. Foss (Springer, Berlin, 2007)
- pp. 1219–1240. ³²N. Z. Liu, D. R. Ladiges, J. Nassios, and J. E. Sader, "Acoustic flows in a slightly rarefied gas," Phys. Rev. Fluids 5, 043401 (2020).
- A. Bokaian, "Natural frequencies of beams under tensile axial loads," J. Sound Vib. 142, 481-498 (1990).